Sustainable Energy & Fuels

ROYAL SOCIETY OF CHEMISTRY

PAPER

View Article Online
View Journal | View Issue

Cite this: *Sustainable Energy Fuels*, 2025, **9**, 6235

Promoting photogenerated charge separation and transfer in a $CuBi_2O_4$ photocathode for improved photoelectrochemical performance

Hasmat Khan,[ab] Alireza Razazzadeh,[a] Myung-Jin Jung,[a] Qi Zhou,[a] Man Sig Lee [c] and Se-Hun Kwon *[ab]

Copper bismuthate ($CuBi_2O_4$) is a fascinating photocathode material for photoelectrochemical (PEC) water-splitting due to its high theoretical photocurrent density and large internal photovoltage. However, its PEC performance is hindered by insufficient light absorption, fast charge carrier recombination, sluggish interfacial charge transfer kinetics, and challenges in achieving uniform photocathode fabrication. Herein, a simple and surfactant-assisted sol–gel method is adopted to fabricate a homogeneous $CuBi_2O_4$ photocathode for improved PEC performance. A small amount of Pluronic P123, a triblock copolymer surfactant, was incorporated into the $CuBi_2O_4$ precursor sol to enhance film homogeneity and modulate the particle size during the sol–gel synthesis process. The experimental results reveal that the addition of the surfactant facilitates uniform deposition of the $CuBi_2O_4$ photocathode and significantly reduces its average particle size from 252 nm to 98 nm. This reduction in particle size results in approximately 2 times higher photocurrent density (−3.8 mA cm^{-2} compared to −2.0 mA cm^{-2}) at 0.2 V *versus* reversible hydrogen electrode (RHE) in 0.1 M Na_2SO_4 electrolyte with an electron scavenger. The enhanced PEC performance originates from the improved charge separation (30.5% at 0.2 V *vs.* RHE) and transfer efficiencies (30.1 V *vs.* RHE) of the surfactant-modulated photocathode. This work provides a straightforward way of fabricating robust, efficient, and large-area CBO photocathodes for PEC application.

Received 3rd August 2025
Accepted 24th August 2025

DOI: 10.1039/d5se01055a

rsc.li/sustainable-energy

Introduction

Solar energy conversion into chemical fuels by the photoelectrochemical (PEC) water-splitting process is an attractive and sustainable strategy to address the global energy crisis.[1–4] In the PEC process, solar energy is directly converted into clean hydrogen fuel without producing any hazardous by-products with the help of a semiconductor photoelectrode and water.[5] The photoelectrode generates charge carriers by absorbing solar energy and the charge carriers are separated and transported to the photoelectrode–electrolyte interface to participate in the water-splitting reactions. Thus, the photoelectrode materials play a key role in light absorption, charge separation, and charge transfer, which determine the overall PEC performance.[6–11]

Several n-type semiconductors as photoanode materials like TiO_2, $BiVO_4$, WO_3, Fe_2O_3, *n*-Si, and *n*-InP[12–16] have been studied and their PEC water oxidation performance evaluated. In contrast, few studies have been reported in the literature on photocathode materials such as CuO, $CuBi_2O_4$, Sb_2Se_3, $CuFe_2O_4$, and $CsPbBr_3$.[17–22] Moreover, the PEC performance of the reported photocathode materials towards the water reduction reaction remains unsatisfactory.

Among the various metal oxide semiconductor-based photocathodes, $CuBi_2O_4$ (CBO), a p-type semiconductor, has attracted special attention for PEC hydrogen production utilizing solar light owing to its favorable band gap energy in the range of 1.5–1.8 eV with a high theoretical photocurrent density close to 20 mA cm^{-2}, suitable conduction band position for the water reduction reaction, and high internal photovoltage.[1,11] However, its PEC properties such as photocurrent density and photostability reported so far were far below the theoretical maximum value.[6] Recent studies have demonstrated that the PEC properties of CBO are mostly limited by the low light absorption efficiency, inferior charge separation and transfer efficiencies, and photocorrosion of the CBO in an aqueous electrolyte solution during PEC measurements.[6,11] In addition, the poor charge separation and transfer efficiencies of CBO originate from its very short charge carrier diffusion length (L_{CD} = 10–52 nm) and high light penetration depth (D_{LP}, 244 nm at the wavelength of 550 nm).[1] Such a large difference between D_{LP}

[a]*School of Materials Science and Engineering, Pusan National University, Busan 46241, Republic of Korea. E-mail: sehun@pusan.ac.kr*

[b]*Institute of Materials Technology, Pusan National University, Busan 46241, Republic of Korea*

[c]*Ulsan Regional Division, Korea Institute of Industrial Technology, Ulsan 44413, South Korea. E-mail: lms5440@kitech.re.kr*

and L_{CD} results in the recombination of photogenerated electron–hole pairs in CBO before they are transferred to the electrode–electrolyte interface. In this regard, many strategies have been explored to ameliorate the above limitations of the CBO photocathode, such as the tuning of morphology, heteroatom doping, heterojunction formation with suitable materials, and surface modification with cocatalysts or noble metals by various synthetic methods like hydrothermal growth, electrodeposition, sol–gel deposition, and spray-pyrolysis.[6–10]

To suppress the rapid charge recombination, nanostructuring of photoelectrodes has been widely accepted as an effective technique to mitigate the problem of short L_{CD}.[11] However, most of the reported CBO photocathodes have inhomogeneous particle size, poor contact with support materials, and small surface area that result in poor PEC performance.[6] In this regard, utilization of surfactant in wet-chemical synthesis routes has greatly been explored to control the shape, size, and porosity of diverse inorganic nanomaterials.[23] Moreover, addition of a small amount of surfactant (that acts as a surface-active agent) in the precursor sol improves the coating homogeneity and makes intimate contact with the substrate and coating materials by overcoming the imbalance in the substrate's surface energy and the surface tension of the sol.[23] Additionally, the surfactants are able to organize themselves by an evaporation-induced self-assembly (EISA) process and prevent fast growth of nanoparticles during the crystallization process.[24] However, the effect of surfactant addition to the precursor sol of CBO on coating homogeneity, particle size, and the fundamental PEC properties (*e.g.*, light absorption, charge separation, and charge transfer efficiencies) has not been thoroughly explored in the literature.

In this work, we report a uniformly deposited CBO photocathode on a fluorine-doped tin oxide (FTO) coated glass substrate by a simple and surfactant assisted sol–gel technique for PEC application. A small amount of Pluronic P123 triblock organic copolymer as surfactant was added in the precursor sol to obtain coating homogeneity and reduce CBO particles size. The CBO photocathode was deposited by drop-casting the precursor sol onto an FTO substrate followed by a subsequent heat treatment at 300 °C for 10 min and 500 °C for 1 h in air. Particle size of CBO was altered by changing the amount of surfactant in the precursor sol. The optimized CBO photocathode with an average particle size of 98 nm showed light absorption, charge separation, and charge transfer efficiencies of ~81%, ~30.5%, and ~30.1%, respectively, which resulted in photocurrent densities of −3.8 mA cm^{-2} and −1.3 mA cm^{-2} at 0.2 V *vs.* RHE in 0.1 M Na_2SO_4 aqueous electrolyte with and without H_2O_2 as an electron scavenger, respectively. This work provides an avenue for fabricating robust, efficient, large-area, and uniform CBO photocathodes for PEC application.

Materials and experimental methods

Preparation of CBO films

A precursor sol for CBO was prepared by dissolving 0.155 g of $Bi(NO_3)_3 \cdot 5H_2O$ (ACS reagent, ≥ 98%, Sigma-Aldrich, USA) and 0.0386 g of $Cu(NO_3)_2 \cdot 3H_2O$ (ACS reagent, ≥ 98%, Sigma-Aldrich, USA) in a mixed solvent of 2-methoxy ethanol (Sigma-Aldrich, anhydrous, 99.8%, Sigma-Aldrich, USA) and acetic acid (ACS reagent, ≥ 99.7%, Sigma-Aldrich, USA) with a volume ratio of 4 : 1. Subsequently, 0.25 mL of acetylacetone (ReagentPlus®, ≥ 99%, Sigma-Aldrich, USA) as a sol-stabilizer was added in the above sol and stirrer for 30 min by using a magnetic stirrer. Then, 10 mg of triblock organic copolymer Pluronic P123 (average $M_n \approx 5800$, Sigma-Aldrich, USA) was added into the above sol as a surfactant and continued to stir for 24 h under ambient conditions to get a homogeneous precursor sol. The homogeneous precursor sol was drop-cast onto a pre-cleaned FTO substrate (735167-1EA, Sigma-Aldrich, USA) and heat treated at 300 °C for 10 min on a hot plate. This process was repeated three times to achieve the optimum CBO film thickness. Finally, the CBO photoelectrode was heated at 500 °C for 1 h under an air atmosphere in a box furnace. The amount of Pluronic P123 in the precursor sol was varied as 5 mg, 10 mg, 15 mg, and 20 mg, and the corresponding CBO films obtained from the respective sols were denoted as CB-P05, CB-P10, CB-P15, and CB-P20, respectively.

Characterization of the fabricated films

The morphology of the CBO photocathodes was studied by scanning electron microscopy (SEM, S-4800, Hitachi, Japan). Transmission electron microscopy (TEM, TALOS F200X (FEI), Thermo Fisher Scientific, USA, operating at 200 kV) was used for structural and elemental analyses of the CBO photocathodes. X-ray diffraction (XRD, D/MAX-2500, Rigaku, Japan) with Cu-Kα radiation at a wavelength of 1.5418 Å was used to observe the crystallinity and crystal phase of the CBO photocathodes. The UV-visible (UV-vis) absorption spectra of the photocathodes were measured using a UV-vis spectrophotometer equipped with an integrating sphere (JASCO, V-770, USA) and the bandgap energies of the photocathodes were estimated from their corresponding UV-vis spectra by using eqn (S1) shown in the SI. X-ray photoelectron spectroscopy (XPS) studies were performed by using a Thermo Electron Corporation (UK) instrument with a spot size of 400 μm, an energy step size of 0.1 eV, and a pass energy of 40 eV to understand the electronic states of the elements in the CBO. The C 1s spectrum with a binding energy of 284.8 eV was used as the reference for all the XPS peaks. Thermogravimetric analysis and differential thermal analysis (TGA-DTA) of the precursor materials for the CBO and CB-P10 samples were conducted using a PerkinElmer STA 8000 Lab system instrument.

Photoelectrochemical measurements

An electrochemical workstation (PGSTAT302N, Metrohm Autolab, Netherlands) with a three-electrode system PEC cell was used for all the PEC measurements. The fabricated CBO photocathode was used as the working electrode (WE), Ag/AgCl (3 M KCl) as a reference electrode (RE), and Pt foil as a counter electrode (CE). A Newport, USA made 100 W xenon arc lamp (LCS-100 solar simulator) equipped with an AM 1.5G filter was used as a light source. A standard solar cell was used to calibrate exactly 1 sun light illumination at the photocathode surface. An

active area of 0.25 cm^2 of the photocathode was considered for PEC measurements with an electrolyte of 0.1 M Na_2SO_4 aqueous solution. Moreover, 0.1 M H_2O_2 as an electron scavenger was mixed into the electrolyte solution of 0.1 M Na_2SO_4. Linear sweep voltammetry (LSV) measurements were performed within the potential range of 0.2–1.0 V *vs.* RHE at a scan rate of 10 mV s^{-1}. The stability test (*J*–*t* curve) of the photocathodes was performed at 0.35 V *vs.* RHE. The electrochemical impedance spectra (EIS) were obtained within a frequency scan range from 5000 Hz to 0.1 Hz at an AC voltage of 5 mV. The open circuit potential (OCP) was measured in 0.1 M Na_2SO_4 aqueous electrolyte under consecutive dark conditions and light illumination. The applied bias photon-to-current conversion efficiency (ABPE) of the photocathodes were calculated from the respective LSV curves using eqn (1):

$$\mathrm{ABPE} = \left(\frac{J(\mathrm{mA\ cm^{-2}}) \times \left(0.2 - V_{\mathrm{appl}}\right)(V)}{P(\mathrm{mW\ cm^{-2}})}\right), \quad (1)$$

where *J* is the photocurrent density, *P* is the light density (100 mW cm^{-2}), and V_{appl} is the applied potential in the RHE. All the applied potentials were converted to those against the RHE using the following Nernst equation (eqn (2)):

$$E_{\mathrm{RHE}} = E^{\circ}_{\mathrm{Ag/AgCl}} + 0.059\ \mathrm{pH} + E_{\mathrm{Ag/AgCl}}, \quad (2)$$

where $E^{\circ}_{Ag/AgCl} = 0.198$ V at 25 °C, pH = 6.7, E_{RHE} = potential *vs.* RHE, and $E_{Ag/AgCl}$ represents the experimental potential *vs.* RE. Moreover, the detailed calculations for the light absorption (η_{abs}), charge separation (η_{sep}), and charge transfer (η_{trans}) efficiencies of the CBO photocathode are provided in the SI file (eqn (S2)–(S9)).

Results and discussion

Structural characterization of the films

The CBO film fabrication procedure is schematically illustrated in Fig. 1(a). A clear and homogeneous precursor sol was drop-cast on a pre-cleaned FTO substrate, subsequently followed by a two-step annealing process at 300 °C for 10 min on a hot plate and 500 °C for 1 h in an air furnace. The crystal structure of the fabricated CBO photocathode was studied by an XRD study (Fig. 1(b)). The XRD pattern shows diffraction peaks at 2-theta values of 20.8, 28.1, 30.6, 33.3, 37.4, 46.7, 53.1, and 55.6° corresponding to the (200), (211), (002), (310), (202), (411), (213) and (332) planes, respectively. These planes represent the kusachiite lattice structure of CBO (JCPDS card no. 42-0334).[1] The XRD result confirms the formation of a highly pure crystalline CBO film on the FTO substrate. The additional XRD peaks at 2-theta values of 26.6, 33.9, 38.0, 51.8, 54.9, 61.7, and 65.8° originated from the FTO layer due to the presence of cassiterite SnO_2 (JCPDS card no. 41-1445).

Moreover, SEM studies of all the CBO, CB-P05, CB-P10, CB-P15, and CB-P20 samples were performed to observe their surface morphology and coating homogeneity (Fig. 1(c–g)). As shown in Fig. 1(c and d) and S1(a), the pristine CBO and CB-P05 films show an inhomogeneous surface with large agglomerated particles. On the other hand, the SEM images of CB-P10, CB-P15, and CB-P20 (Fig. 1(e–g)) show homogeneous film surfaces with reduced particle size after increasing the amount of Pluronic P123 surfactant in the precursor sol of CBO. Moreover, the low-magnification SEM image of the CBO film surface shows coating defects whereas the CB-P10 exhibits a large-area homogeneous film surface (Fig. S1(a and b)). The average particle sizes of the CBO (252 nm), CB-P05 (170 nm), CB-P10 (98 nm), and CB-P15 (155 nm) films were calculated from their respective SEM images and the histogram graphs of the particles size distribution are shown in Fig. S2(a–d). It seems that the higher amount of surfactant in the precursor sol resulted in agglomerated CBO particles (Fig. 1(f and g)). The coating defect in the CBO film surface as shown in Fig. S1(a) may have appeared due to the trapped air in the coating layer, resulting in air-based coating defects.[25,26] It is noted that the homogeneous film can be deposited by matching the surface energy of the substrate and the surface tension of the sol. Adding a small amount of surfactant to the precursor sol overcomes the mismatch between the surface energy of the substrate and the surface tension of the sol, resulting in a homogeneous coating. Also, the surfactant in the precursor sol is capable of organizing itself by an EISA process and generates different organized structures (such as micellar, lamellar *etc.*) that provide a dynamic solid–liquid interface during the crystallization process, as well as preventing fast growth of nanoparticles, leading to smaller particle size. In addition, the surfactant left some mesopores after heat treatment that provide a large specific surface area.[25] From the histogram graphs of the particles size distribution in Fig. S2(a–d), it can be elucidated that the CB-P10 sample exhibited the lowest average particle size compared with other samples. The large particle size limits the PEC performance by rapid photogenerated charge recombination. However, it is worth noting that the particle size within the range of $<2L_{CD}$ of a photocatalyst improves charge separation efficiency by suppressing charge recombination.[11,27] Therefore, we altered the particle size of CBO photocathodes by carefully changing the surfactant loading in the precursor sol and checked the photocurrent densities of different CBO photocathodes by LSV measurement (Fig. S3). It was observed that the CB-P10 sample with an average particle size of 98 nm falls within the range of $<2L_{CD}$ (L_{CD} = 10–52 nm for CBO), resulting in improvement in photocurrent density. However, the crystal phase of the different CBO photocathodes remains the same after loading Pluronic P123 surfactant as evident from the XRD measurement (Fig. S4). It is noted that an increased number of grain boundaries along the thickness direction of CBO films can hinder PEC performance due to elevated charge transfer resistance at grain boundaries. However, the overall PEC performance for water reduction is governed by the product of four interdependent factors: (i) the theoretical maximum photocurrent density of the CBO semiconductor, (ii) light absorption efficiency, (iii) photogenerated charge separation efficiency, and (iv) interfacial charge transfer efficiency. While smaller grain sizes can impede charge transfer by introducing more grain boundaries, they can simultaneously enhance charge separation efficiency by suppressing bulk recombination. This is particularly relevant for CBO, which

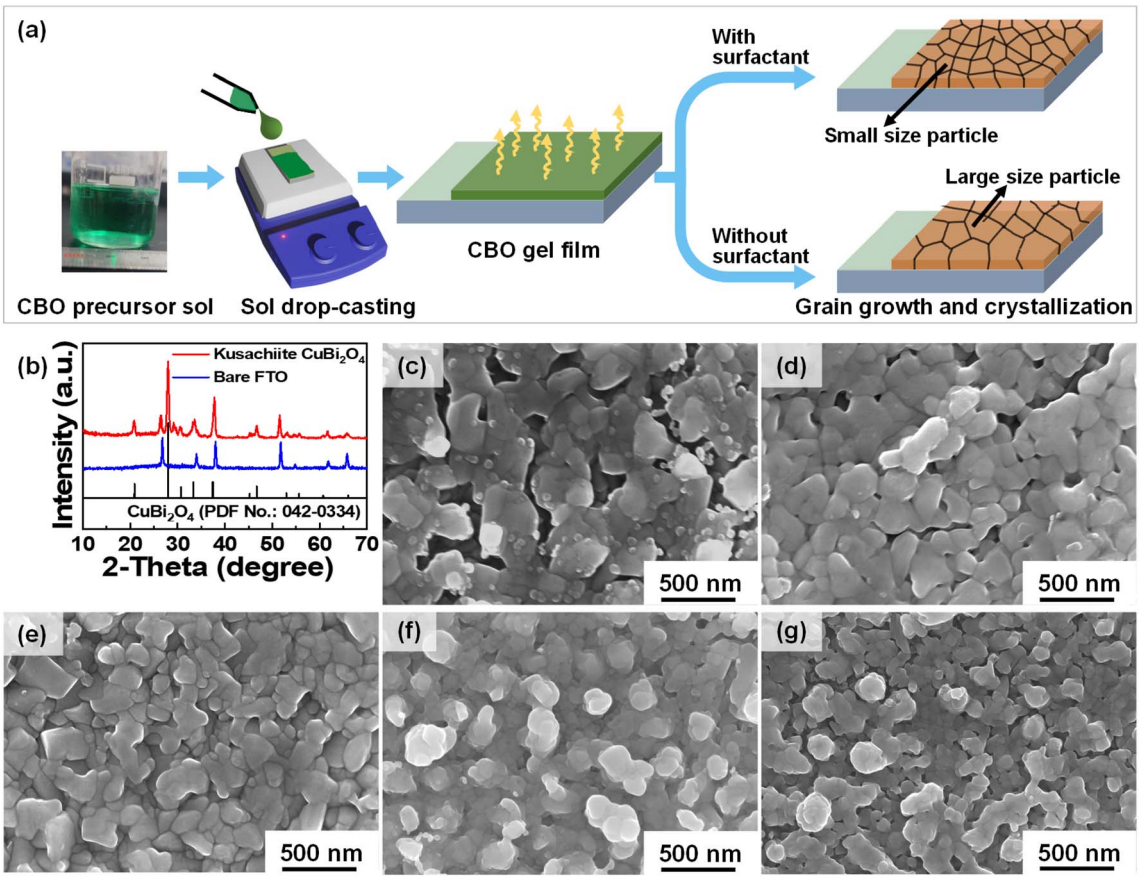

Fig. 1 (a) Schematic diagram of the fabrication steps of the CBO photocathode. (b) XRD patterns of bare FTO and CBO. (c–g) top-view SEM images of CBO, CB-P05, CB-P10, CB-P15, and CB-P20 films, respectively.

suffers from a short carrier diffusion length. In such cases, nanostructuring and particle size tuning become crucial, as they allow photogenerated carriers to reach the semiconductor/electrolyte interface before recombination occurs. Indeed, several studies have reported improved PEC performance upon nanostructuring of CBO-based photocathodes.[5,6,9]

To support this, cross-sectional SEM analysis of all CBO films (CBO, CB-P05, CB-P10, CB-P15, and CB-P20) was conducted and shown in Fig. 2(a–e). The images reveal that all films, except CB-P20, exhibit comparable thicknesses (~500 nm). CB-P20 has a slightly increased thickness (~550 nm), likely due to the higher content of Pluronic P123 surfactant, which increases sol viscosity and results in a thicker coating during the sol–gel dip-coating process. Notably, the CBO and CB-P05 samples consist of inhomogeneous large and small particles. In contrast, CB-P10 displays a more uniform morphology with homogeneous particle distribution (Fig. 2(a–c)). However, further increasing the surfactant concentration in CB-P15 and CB-P20 led to particle agglomeration (Fig. 2(d and e)), which we believe contributes to reduced PEC activity due to increased charge recombination and hindered mass transport. Additionally, SEM-EDX elemental mapping and quantitative analysis of CB-P10 confirmed the presence of Cu, Bi, and O elements on the FTO substrate (Fig. 2(f–j)), validating the film composition.

TEM microstructural analyses were performed with the CB-P10 sample as shown in Fig. 3(a–f). The interplanar distance of the sample was calculated from the HRTEM image (Fig. 3(a)) and the calculated *d*-spacing of ~0.32 nm corresponds to the (211) plane (Inset, Fig. 3(a)) of kusachiite CBO.[1,5] This TEM result supports the XRD data. Also, selected area electron diffraction (SAED) patterns (Fig. 3(b)) were recorded to analyze the crystal information and the calculated crystal planes well matched with the XRD data (Fig. 1(b)) along with the lattice fringes obtained from the HRTEM image. In addition, the high-angle annular dark-field (HAADF) image (Fig. 3(c)) and its corresponding energy-dispersive spectroscopy (EDS) elemental-mapping images (Fig. 3(d–f)) confirm the presence of Cu, Bi, and O elements in the CB-P10 sample. Moreover, TGA-DTA analyses of the precursor materials were conducted to check the possible presence of residual surfactants in the CB-P10 photocathode after the calcination process. The TGA-DTA results clearly show that the decomposition of carbonaceous components, including any potential organic surfactants, is completed by approximately 400 °C (Fig. S5(a and b)). Furthermore, the crystallization of $CuBi_2O_4$ occurs at around 450 °C and then no mass loss occurred up to 700 °C. From the TGA curves, we calculated weight loss of the precursor materials at 500 °C and found it to be ~30.11% and ~35.63% for CBO and CB-P10

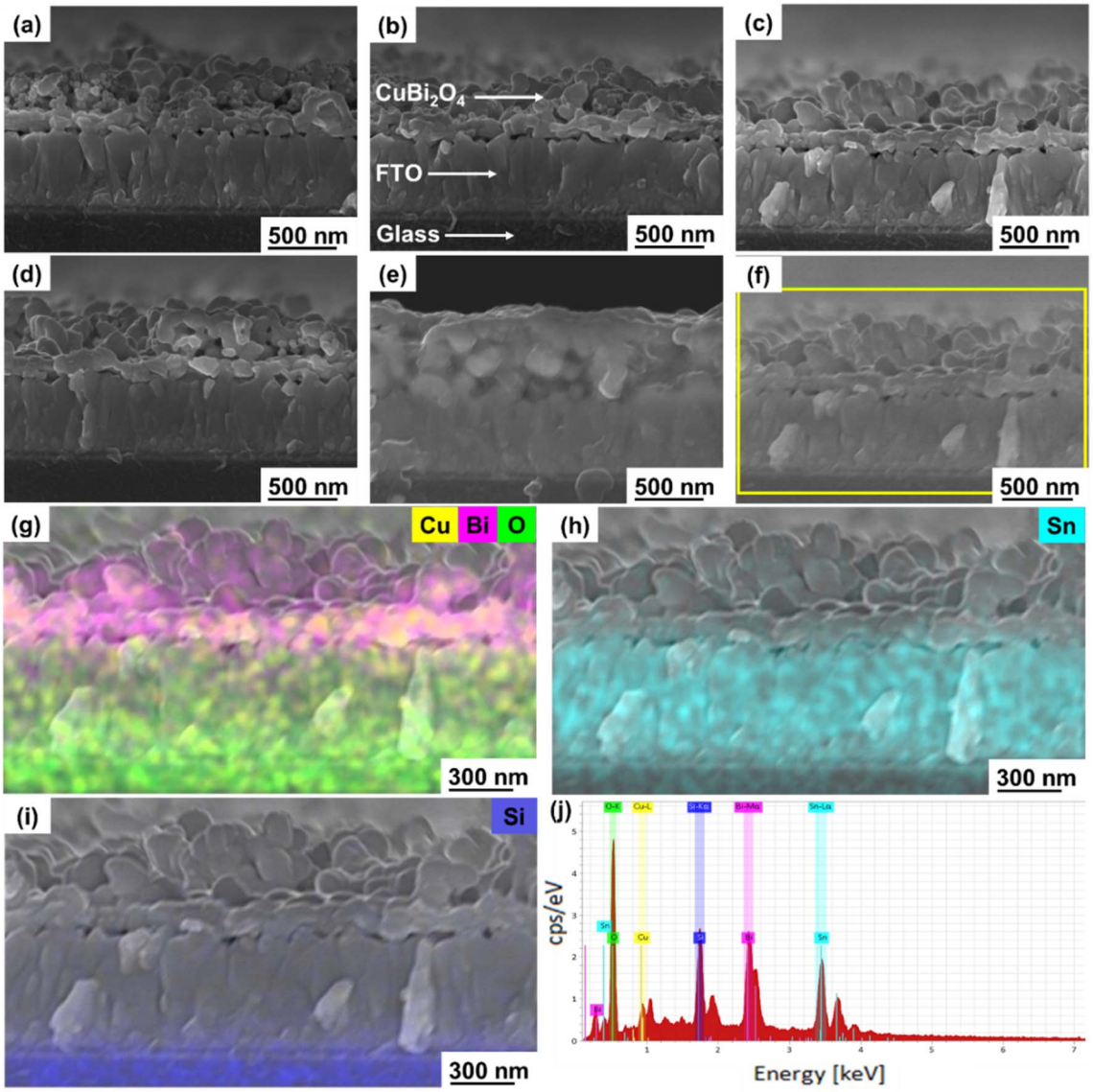

Fig. 2 Cross-sectional SEM images of all CBO films: (a) CBO, (b) CB-P05, (c) CB-P10, (d) CB-P15, and (e) CB-P20. (f–j) SEM–EDX elemental mapping and quantitative analysis of the CB-P10 sample.

precursor materials, respectively (Fig. S5(a and b)). The slightly higher weight loss of the CB-P10 could be attributed to the removal of Pluronic P123 surfactant from the precursor material. Based on this, the calcination temperature of 500 °C for 1 h used in our synthesis protocol is sufficient to ensure complete removal of any organic residues. TEM measurement was also conducted to check the possible presence of residual surfactants in the CB-P10 sample after curing at 300 °C and 500 °C. Bright-field TEM images combined with TEM-EDS elemental mapping of the sample cured at 300 °C reveal a noticeable presence of carbon, indicating the incomplete decomposition of organic constituents at this temperature (Fig. S6(a–h)). In contrast, the CB-P10 sample annealed at 500 °C for 1 h shows no detectable carbon residue in the corresponding bright-field TEM images and TEM-EDS analysis (Fig. S7(a–h)), suggesting effective thermal decomposition and removal of the surfactant residues during calcination.

XPS studies were further performed to determine the electronic states of the elements present in the CBO and CB-P10 samples (Fig. 4(a–c)). The XPS survey spectrum demonstrates that the fabricated sample is composed of Cu, Bi, and O elements (Fig. S8) and the presence of the Sn 3d binding energy peak originated from the FTO layer. The high-resolution XPS spectrum for Cu 2p binding energy peaks appeared at 953.9 eV and 933.7 eV for the two spin–orbit peaks of Cu $2p_{1/2}$ and Cu $2p_{3/2}$, respectively with the satellite peak at around 941–944 eV (Fig. 4(a)), confirming the existence of Cu^{2+}.[27] The binding energy peaks for Bi $4f_{7/2}$ (158.6 eV) and $4f_{5/2}$ (163.9 eV) are the characteristic binding energy peaks of Bi^{3+} in CBO (Fig. 4(b)).[3,27] For O 1s high-resolution spectra, two prominent peaks at 529.5 eV and 531.1 eV are observed (Fig. 4(c)). These two O 1s peaks can be attributed to the lattice oxygen (529.5 eV) and oxygen vacancy (531.1 eV) in the CB-P10.[5,7] The comparison of the core-level binding energies of Cu 2p, Bi 4f, and O 1s spectra is nearly

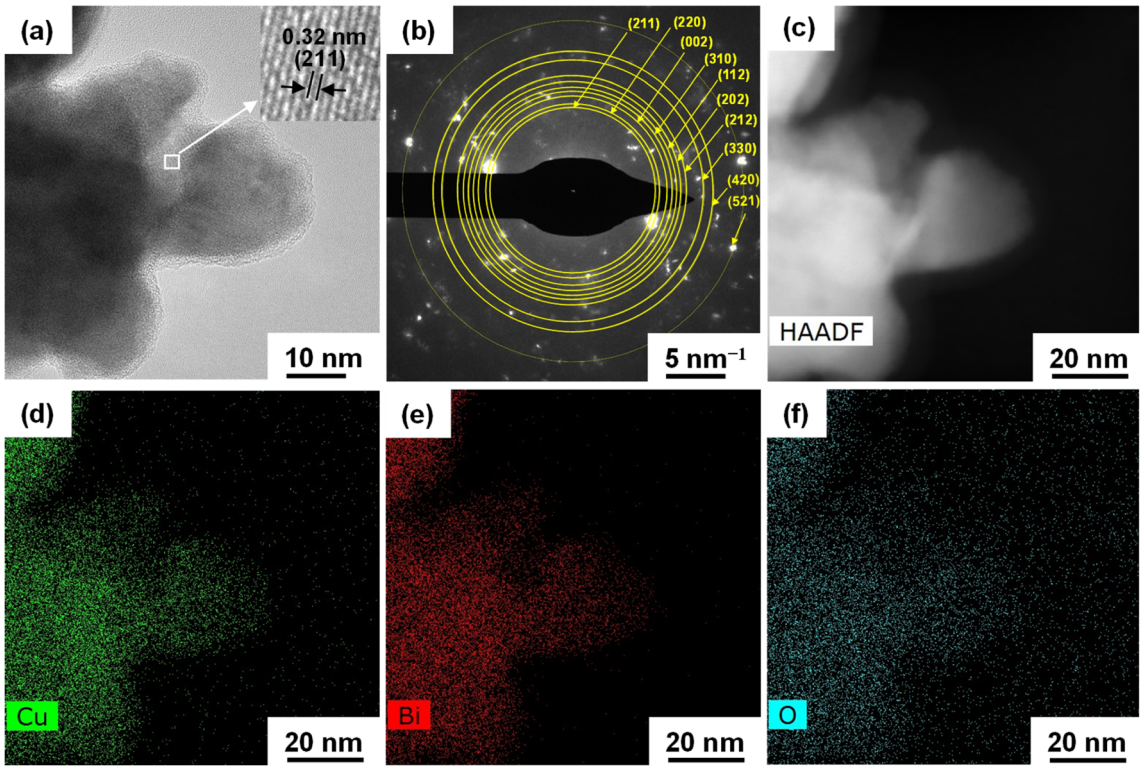

Fig. 3 TEM studies of the CB-P10 sample; (a) bright field TEM image, (b) SAED patterns, (c) HAADF image, and (d–f) EDS-elemental mapping images of Cu, Bi, and O elements, respectively. Inset of (a) represents the lattice fringe obtained from the square marked area in (a).

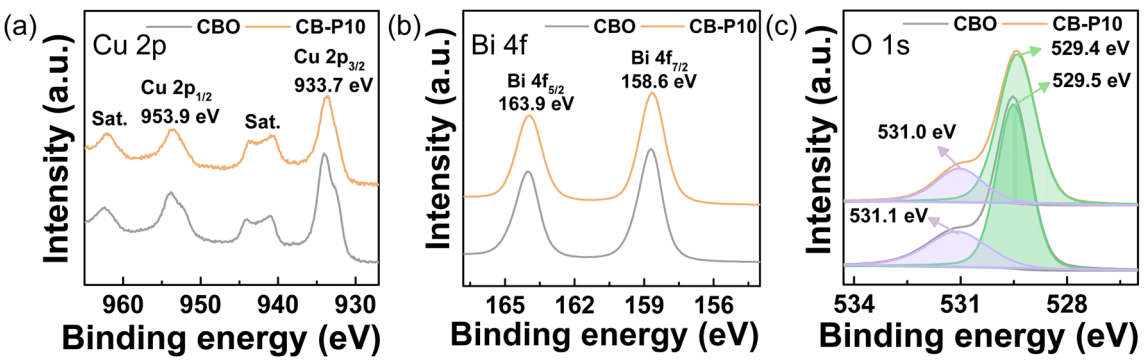

Fig. 4 XPS high-resolution spectra of CBO and CB-P10 samples; (a) Cu 2p, (b) Bi 4f, and (c) O 1s binding energy peaks.

identical for both the CBO and CB-P10 samples, indicating no significant change in the surface chemical states upon the addition of Pluronic P123. Additionally, the binding energy of the reference C 1s peak (~284.8 eV) remained consistent for both the CBO and CB-P10 samples, and no significant additional carbon-related peaks (*e.g.*, from residual organics or surfactants) were detected (Fig. S9). This further confirms the absence of residual surfactants after calcination.

Photoelectrochemical studies

The PEC measurements were conducted in an undivided three-electrode system cell in 0.1 M Na_2SO_4 aqueous electrolyte. The LSV curves for CBO and CB-P10 samples were obtained by the potential scan varied from 0.2 V to 1.0 V *vs.* RHE under continuous light illumination, chopped and dark conditions to confirm the effect of light on the photoelectrode surface (Fig. 5). The CBO photocathode exhibited a photocurrent density of −0.62 mA cm^{-2} at 0.2 V *vs.* RHE whereas the same sample showed a photocurrent density of −2.0 mA cm^{-2} at 0.2 V *vs.* RHE in the presence of H_2O_2 as an electron scanvenger in the electrolyte solution (Fig. 5(a)). On the other hand, the CB-P10 sample showed around two times higher photocurrent density (−1.3 mA cm^{-2} at 0.2 V *vs.* RHE) compared to that of the CBO sample in 0.1 M Na_2SO_4 aqueous electrolyte. Notably, a much higher photocurrent density of −3.8 mA cm^{-2} at 0.2 V *vs.* RHE with an onset potential of ~0.8 V *vs.* RHE was exhibited by the

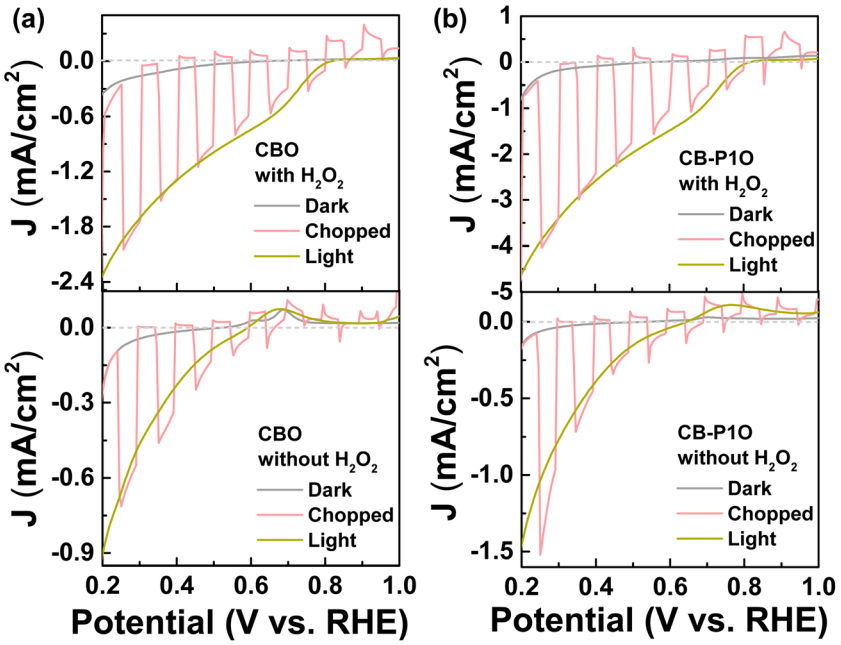

Fig. 5 LSV curves of CBO and CB-P10 photoelectrodes; (a) CBO and (b) CB-P10. The LSV curves measured under dark, light, and chopped conditions in 0.1 M Na_2SO_4 aqueous electrolyte with/without the H_2O_2 electron scavenger.

CB-P10 sample in the presence of the electron scavenger in the electrolyte (Fig. 5(b)). The photocurrent values were estimated from the LSV curves by subtracting the dark current from the illuminated current at each potential. We believe that the higher photocurrent density of the CB-P10 sample originated from the film homogeneity and its reduced average particle size (98 nm) compared to that of the CBO sample (252 nm). As the L_{CD} of CBO is only 10–52 nm, larger particle size limits its PEC performance by increasing the bulk recombination rate of photogenerated charge carriers.[6,11] Moreover, XPS studies (Fig. 4(a–c)) suggest that the enhanced PEC performance of CB-P10 is primarily due to morphological improvements rather than changes in surface chemistry. Moreover, the ABPE values of CBO and CB-P10 photocathodes were calculated using eqn (1) from their corresponding LSV curves and the values are 0.05% and 0.08% at ~0.35 V *vs.* RHE (without the electron scavenger) and 0.30% and 0.60% at ~0.56 V *vs.* RHE (with the electron scavenger), respectively (Fig. S10). A comparative analysis was incorporated in Table S1, SI to contextualize our findings within the existing literature. Relevant studies on $CuBi_2O_4$-based photocathodes were cited and discussed in terms of synthesis method, photocurrent density, and onset potential.

EIS measurement was performed to analyse the charge transfer behavior of the samples. Fig. 6(a) exhibits the EIS curves of the CBO and CB-P10 samples and the arc radius of the CB-P10 photocathode is smaller than that of the CBO photocathode, suggesting easier photogenerated charge transfer at the photoelectrode–electrolyte interface. The easier charge transfer of CB-P10 could be attributed to the smaller particle size of the sample.[28] Moreover, we measured the open-circuit potential (OCP) under dark and light illumination. The difference in OCP under dark and light (ΔOCP) represents the

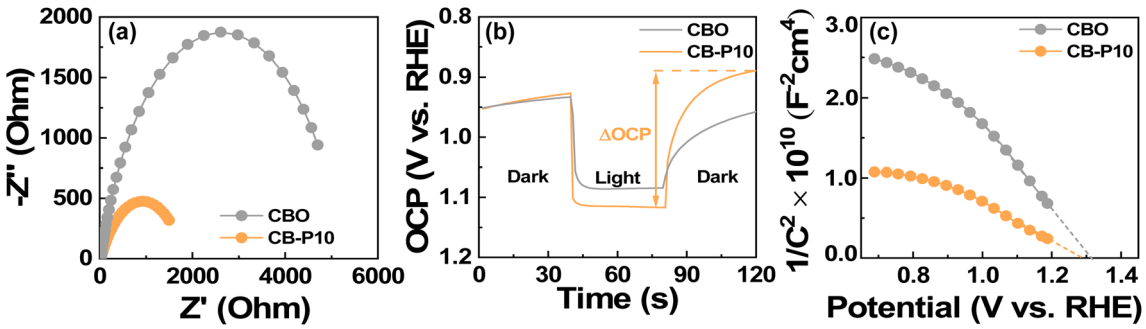

Fig. 6 (a) EIS Nyquist plot of CBO and CB-P10 photocathodes measured at 0.35 V *vs.* RHE in 0.1 M Na_2SO_4 aqueous electrolyte under 1 sun illumination, (b) OCP measured under dark and light conditions and (c) the Mott–Schottky plot showing the negative slope of the photoelectrodes.

amount of band bending in the semiconductor materials. Fig. 6(b) shows the ΔOCP values for CBO and CB-P10 are ~0.12 and ~0.23 V, respectively. The higher ΔOCP value for CB-P10 suggests more band flattening under illumination, implying better photogenerated charge separation.[1,24] Moreover, the Mott–Schottky (M–S) curves (Fig. 6(c)) display a negative slope for both the CBO and CB-P10 samples, confirming their p-type semiconducting nature.[23] Notably, the smaller particle size of CB-P10 may lead to a larger surface area, which could in turn affect the impedance behavior. However, the interpretation of a smaller Nyquist arc in our case cannot be attributed solely to the surface area effect. Although increased surface area generally reduces charge-transfer resistance due to the availability of more active sites, our interpretation was also supported by additional evidence from M–S analysis and PEC performance. The CB-P10 sample not only showed a smaller Nyquist arc but also exhibited a flatter M–S plot slope (Fig. 6(c)), suggesting a higher donor density, which is directly related to the enhanced charge carrier transport.[29,30] This indicates that the enhanced charge transfer is not merely a consequence of surface area differences but also reflects the intrinsic electronic properties of the material. Moreover, to decouple surface area effects from intrinsic charge transfer behavior, we performed PEC measurements under identical experimental conditions. The consistent improvement in transient photocurrent responses and linear sweep voltammetry (Fig. 5(a and b)) of CB-P10 further supports that the observed impedance trend is due to better interfacial charge transfer rather than surface area alone.

In order to gain deeper insight into the effect of CBO particle size on its fundamental PEC properties such as η_{abs}, η_{sep}, and η_{trans} efficiencies, we firstly measured the UV-vis absorption properties of the films (Fig. 7(a)). From the UV-vis curves, it seems that a slight absorption onset appears at ~800 nm followed by a more prominent onset near 695 nm. The band gap energy values of the CBO (1.83 eV) and CB-P10 (1.80 eV) (Inset, Fig. 7(a)) films were calculated using the Tauc equation (eqn (S1)) and these values are well matched with the reported band gap energy value of CBO.[3] Moreover, light harvesting efficiencies (LHE) of the films were estimated from their respective UV-vis absorption curves using eqn (S2) and shown in Fig. 7(b). To get the η_{abs} value, we calculated the theoretical maximum photocurrent density (J_{max}) and integrated absorption photocurrents (J_{abs}) (Fig. S11) of the CBO and CB-P10 photocathodes with the help of eqn (S3) and (S4), respectively. Then, we estimated the η_{abs} *vs.* wavelength curve (Inset, Fig. 7(b)) for CBO and CB-P10 samples using eqn (S5). The η_{abs} values for the CBO and CB-P10 at 1.83 eV and 1.80 eV were calculated to be ~79% and ~81%, respectively. It is noted that the photocurrent generated by water-splitting reactions (J_{water}) can be expressed by the products of J_{max}, η_{abs}, η_{sep}, and η_{trans} (eqn (S6)). In addition, it is reported that the η_{trans} of the semiconductor photocathodes can be obtained as 100% by using an electron scavenger such as hydrogen peroxide (H_2O_2) in the electrolyte solution because it utilizes all the photoelectrons that reached the surface for the H_2O_2 reduction reaction.[1,3] Therefore, eqn (S6) can be written as eqn (S7) and plotted as the ($\eta_{abs} \times \eta_{sep}$) *vs.* potential curve as shown in Fig. S12. Subsequently, we estimated the η_{sep} values of ~16.5% and ~30.5% for CBO and CB-P10 samples, respectively at 0.2 V *vs.* RHE from eqn (S8) and Fig. 7(c). Finally, the η_{trans} values of the samples for the water

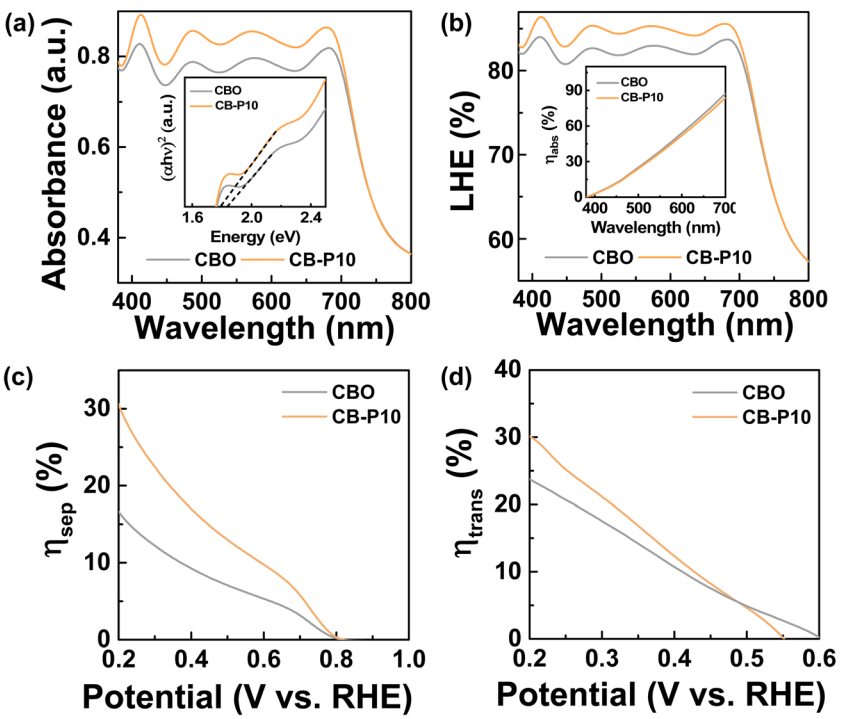

Fig. 7 (a) UV-vis absorption spectra, (b) LHE plot obtained from the absorption curves, (c) the η_{sep}, and (d) the η_{trans} of the CBO and CB-P10 photocathodes. Insets of (a and b) represent the Tauc plot for band gap energy determination and the η_{abs} *vs.* wavelength plot, respectively.

reduction reaction were calculated with the help of eqn (S9) and the η_{trans} values were ~23.7% for CBO and ~30.1% for CB-P10 at 0.2 V *vs.* RHE (Fig. 7(d)). The above results show that the CB-P10 sample with smaller particle size facilitated the enhancement of the η_{sep} and η_{trans}, leading to an improvement in its PEC performance. Our previously reported works also showed that nanostructuring and particle size reduction of photoelectrodes improved their η_{sep} and η_{trans}.[23,27,28] Therefore, proper nanostructuring and particle size tuning could greatly improve the PEC performance of CBO-based photocathodes.

Furthermore, we performed the stability test of the CBO and CB-P10 photocathodes in 0.1 M Na_2SO_4 aqueous electrolyte with/without H_2O_2 as an electron scavenger in a three-electrode system PEC cell at 0.35 V *vs.* RHE. The photocurrent densities decrease from −0.95 mA cm^{-2} to −0.08 mA cm^{-2} and from −1.17 mA cm^{-2} to −0.16 mA cm^{-2} for the CBO and CB-P10 samples, respectively within 12 min of testing in 0.1 M Na_2SO_4 electrolyte (Fig. 8(a) and Inset, Fig. 8(a)). To examine the surface chemical states of the CB-P10 photocathode after the stability test, XPS analysis was performed. The high-resolution XPS spectrum of Cu 2p (Fig. S13(a)) shows the binding energy peaks at around 932.7 eV (Cu $2p_{3/2}$) and 952.6 eV (Cu $2p_{1/2}$) which are shifted to lower binding energy compared to the Cu 2p peaks (933.7 eV and 953.9 eV for Cu $2p_{3/2}$ and Cu $2p_{1/2}$ states, respectively) of the sample before the stability test (Fig. 4(a)). The shifting of Cu 2p peaks to lower binding energy indicates the self-reduction or photocorrosion of the CB-P10 sample after the stability test.[7]

Moreover, the XPS spectrum of Bi 4f exhibits the major peaks at around 159.3 eV (Bi $4f_{7/2}$) and 164.6 eV (Bi $4f_{5/2}$) which are slightly shifted to higher binding energies compared to the sample before stability.[1] In addition, small shoulder peaks at lower binding energies of 157.5 eV and 163.0 eV for Bi $4f_{7/2}$ and Bi $4f_{5/2}$ states, respectively, appeared after the stability test (Fig. S13(b)). Moreover, the O 1s spectrum obtained after the stability test shows a significant increase in the peak intensity centered at 531.4 eV (Fig. S13(c)), which can be attributed to the adsorbed H_2O and/or hydroxyl groups at the surface of the sample.[1,7] XRD study was also performed with the CB-P10 sample after the stability test (Fig. S14). In addition to the

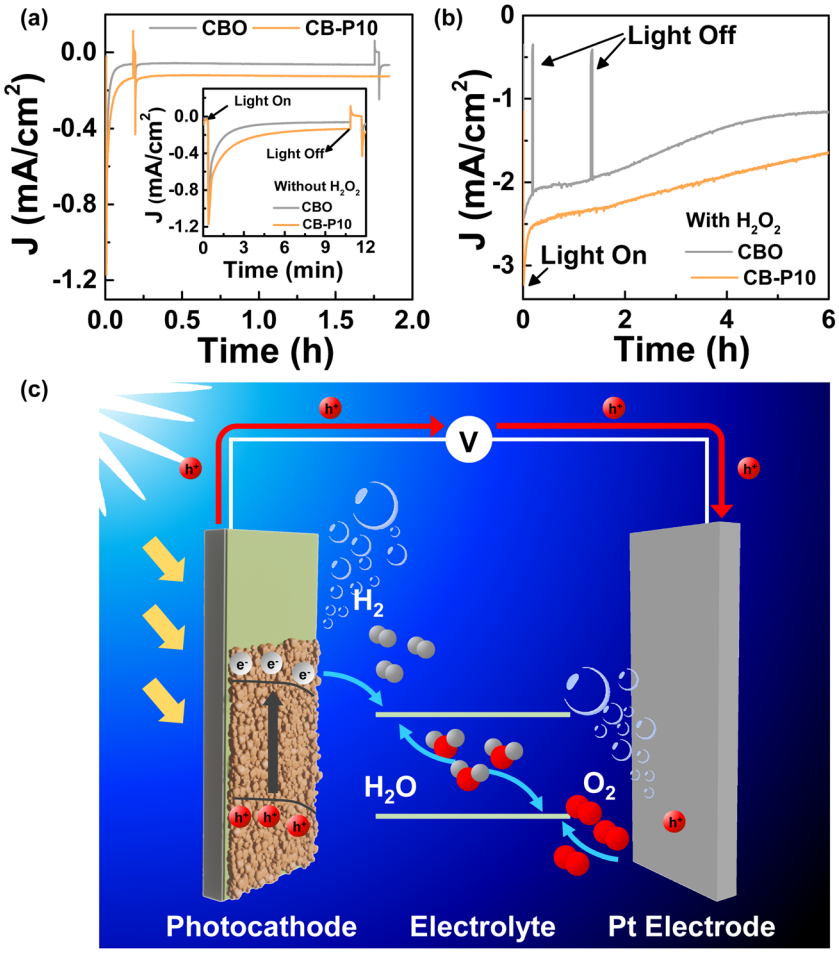

Fig. 8 PEC stability test at 0.35 V *vs.* RHE; (a) chronoamperometric (*J*–*t*) curves for CBO and CB-P10 photocathodes measured in 0.1 M Na_2SO_4 aqueous electrolyte, (b) the *J*–*t* curves of the same photocathodes were measured in the presence of an electron scavenger (H_2O_2) in the 0.1 M Na_2SO_4 aqueous electrolyte, and (c) a schematic diagram showing the PEC water reduction mechanism at the CBO photocathode surface under light illumination. Inset of (a) presents the enlarged stability curves of the samples, show rapid photocurrent decay with time.

characteristic diffraction peaks of kusachiite Cu_2BiO_4 and cassiterite SnO_2 from the FTO substrate, new diffraction peaks emerged at 2-theta values of 53.5°, and 61.8°, corresponding to the (200) and (220) planes of Cu_2O (JCPDS card no. 03-0898), respectively.[3,7,31] The appearance of the Cu_2O phase likely originates from the photocorrosion of Cu_2BiO_4 during prolonged PEC operation. However, the photocathodes showed improved stability in the presence of an electron scavenger in the electrolyte as shown in Fig. 8(b). Both the CBO and CB-P10 photocathodes showed around 50% decay in photocurrent density after 6 h of measurement. In the presence of an electron scavenger in the electrolyte, the photogenerated electrons are rapidly scavenged to the electrode–electrolyte interface and injected into protons.[9] However, in the absence of the electron scavenger the photogenerated electrons accumulate at the electrode–electrolyte interface and photoreduce the surface Cu^{2+} in CBO instead of water photoreduction and cause photocorrosion.[1,9] Under the PEC conditions, both the Cu^{2+} and Cu^{+} are unstable due to their more positive reduction potential compared to the reduction potential of the H^{+} ion.[1] Therefore, bare CBO could not produce stable photocurrent for PEC water reduction to H_2. However, the enhanced photocurrent observed for the CB-P10 sample during H_2O_2 reduction suggests that the photocathode's stability toward water reduction could be significantly improved by introducing an appropriate cocatalyst overlayer. Such a layer would facilitate efficient interfacial charge transfer by effectively capturing photogenerated electrons reaching the surface, thereby promoting the desired reduction reaction and mitigating the photocorrosion issue.

Based on the above experimental results, a schematic drawing was performed to show the water reduction to H_2 at the CBO photocathode surface and water oxidation to O_2 gas at the Pt surface (Fig. 8(c)) under the PEC conditions. Under light illumination, the CBO photocathode absorbs light and generates photogenerated electrons in the conduction band (CB) and holes in the valence band (VB). Subsequently, the photogenerated electrons transfer to the CBO-electrolyte interface for water reduction to H_2 and the photogenerated holes transfer through the back-contact of the CBO and reach to the Pt surface *via* an externally connected wire for water oxidation to O_2 gas.[3,9] The above experimental results show that a small amount of surfactant in the precursor sol allowed homogeneous coating of the CB-P10 photocathode by overcoming the air-based coating defects and facilitated a dynamic solid–liquid interface during the crystallization process that prevented fast growth of nanoparticles, leading to a decrease in particle size. The CB-P10 photocathode with smaller particle size compared to that of the CBO photocathode contributed to suppressing charge carriers' recombination and promoting charge separation efficiency. The combined effects of coating homogeneity and enhanced charge separation efficiency led to an improvement in the PEC performance of the CB-P10 photocathode. For practical application of CBO-based photocathodes, further improvements in photocurrent and photostability for water-splitting reactions are required. However, the reduction potential of the Cu^{2+} ion is more positive than the water reduction potential that causes the photoreduction of the Cu^{2+} ion in CBO during the long-term PEC measurement. Moreover, the CBO photocathode accumulates photogenerated electrons at the surface due to its inferior interfacial (electrode–elecrolyte) reaction kinetics that induces severe photocorrosion. Therefore, the incorporation of a suitable electrocatalyst or cocatalyst overlayer on the CBO photocathode is essential to effectively extract and utilize the surface-accumulated charges, thereby accelerating interfacial charge transfer kinetics and enhancing overall PEC performance. However, the current study does not encompass the investigation of cocatalyst-modified $CuBi_2O_4$ photocathodes, and thus this aspect remains beyond the scope of the present work.

Conclusions

In this study, we have fabricated a CBO photocathode by a surfactant-assisted sol–gel method for checking its PEC performance. An organic block co-polymer (Pluronic P123) was used as a surfactant in the precursor sol of CBO to obtain coating homogeneity by overcoming the air-based coating defects in the photocathode. Moreover, the surfactant facilitated a dynamic solid–liquid interface during the crystallization process that prevented fast growth of nanoparticles, leading to a decrease in CBO particle size. The experimental results reveal that the addition of the surfactant facilitates uniform deposition of the $CuBi_2O_4$ photocathode and significantly reduces its average particle size from 252 nm to 98 nm. This reduction in particle size results in approximately 2 times higher photocurrent density (-3.8 mA cm^{-2} compared to -2.0 mA cm^{-2}) at 0.2 V *vs.* RHE in 0.1 M Na_2SO_4 electrolyte with an electron scavenger. The enhanced PEC performance originates from the improved charge separation (30.5% at 0.2 V *vs.* RHE) and transfer efficiencies (30.1% at 0.2 V *vs.* RHE) of the surfactant-assisted photocathode. The enhanced photocurrent for H_2O_2 reduction indicates that the photocathode's stability for water reduction could be improved by overcoating a suitable cocatalyst, which would enhance interfacial charge transfer, promote reduction reactions, and suppress photocorrosion. This work will serve as a foundation for the fabrication of efficient and large-area CBO-based photocathodes for PEC applications.

Author contributions

H. Khan: conceptualization, writing – original draft, visualization, investigation, formal analysis, data curation. A. Razazzadeh: visualization, investigation, formal analysis. M.-J. Jung: visualization, investigation. Q. Zhou: materials characterization and formal analysis. M. S. Lee: supervision, funding acquisition. S.-H. Kwon: manuscript editing, supervision, funding acquisition, conceptualization.

Conflicts of interest

The authors declare that they have no known competing financial interests or personal relationships that could have appeared to influence the work reported in this paper.

Data availability

The data supporting this article have been included as part of the SI. Supplementary information: PEC calculations, SEM studies, LSV, XRD, TGA-DTA, TEM, XPS, ABPE, and integrated photocurrent density. See DOI: https://doi.org/10.1039/d5se01055a.

Acknowledgements

This work was supported by the Commercialization Promotion Agency for R&D Outcomes (COMPA) grant funded by the Korean Government(Ministery of Science and ICT) (Grant RS-2023-00304764), by the National Research Foundation of Korea (NRF) grant funded by the Korean Government (MIST) (Grant RS-2023-00271685621820653000002), and by the 2023 BK21 FOUR Program of Pusan National University.

References

1 S. P. Berglund, F. F. Abdi, P. Bogdanoff, A. Chemseddine, D. Friedrich and R. van de Krol, Comprehensive evaluation of $CuBi_2O_4$ as a photocathode material for photoelectrochemical water splitting, *Chem. Mater.*, 2016, **28**, 4231–4242.

2 J. K. Cooper, Z. Zhang, S. Roychoudhury, C.-M. Jiang, S. Gul, Y.-S. Liu, R. Dhall, A. Ceballos, J. Yano, D. Prendergast and S. E. Reyes-Lillo, $CuBi_2O_4$: Electronic structure, optical properties, and photoelectrochemical performance limitations of the photocathode, *Chem. Mater.*, 2021, **33**, 934–945.

3 D. Kang, J. C. Hill, Y. Park and K.-S. Choi, Photoelectrochemical properties and photo stabilities of high surface area $CuBi_2O_4$ and Ag-doped $CuBi_2O_4$ photocathodes, *Chem. Mater.*, 2016, **28**, 4331–4340.

4 L. Chen, J. Yang, S. Klaus, L. J. Lee, R. Woods-Robinson, J. Ma, Y. Lum, J. K. Cooper, F. M. Toma, L. Wang, I. D. Sharp, A. T. Bell and J. W. Ager, p-Type transparent conducting oxide/n-type semiconductor heterojunctions for efficient and stable solar water oxidation, *J. Am. Chem. Soc.*, 2015, **137**, 9595–9603.

5 B. Meena, M. Kumar, R. K. Hocking, S. Juodkazis, V. Biju, P. Subramanyam and S. Challapalli, Exploring $CuBi_2O_4$ as a promising photocathode material for PEC water splitting, *Energy Fuels*, 2023, **37**, 14280–14289.

6 G. Seo, B. Kim, S. W. Hwang, S. S. Shin and I. S. Cho, High-performance bulky crystalline copper bismuthate photocathode for enhanced solar water splitting, *Nano Energy*, 2021, **80**, 105568.

7 K. Wakishima, T. Higashi, A. Nagaoka and K. Yoshino, Photoelectrochemical properties of p-type $CuBi_2O_4$ prepared by spray pyrolysis of carbon-free precursor aqueous solution combined with post-annealing treatment, *New J. Chem.*, 2024, **48**, 131–143.

8 S. Bera, S. A. Lee, C.-M. Kim, H. Khan, H. W. Jang and S.-H. Kwon, Controlled Synthesis of Vertically Aligned SnO_2 NanograssStructured Thin Films for $SnO_2/BiVO_4$ Core–Shell Heterostructures with Highly Enhanced Photoelectrochemical Properties, *Chem. Mater.*, 2018, **30**, 8501–8509.

9 D. A. Reddy, Y. Kim, P. Varma, M. Gopannagari, K. A. J. Reddy, D. H. Hong, I. Song, D. P. Kumar and T. K. Kim, Inverse opal $CuBi_2O_4$ photocathodes for robust photoelectrochemical water splitting, *ACS Appl. Energy Mater.*, 2022, **5**, 6050–6058.

10 F. Wang, W. Septina, A. Chemseddine, F. F. Abdi, D. Friedrich, P. Bogdanoff, R. v. d. Krol, S. D. Tilley and S. P. Berglund, Gradient self-doped $CuBi_2O_4$ with highly improved charge separation efficiency, *J. Am. Chem. Soc.*, 2017, **139**, 15094–15103.

11 M. Li, X. Tian, X. Zou, X. Han, C. Du and B. Shan, Promoting photoelectrochemical hydrogen evolution activity of $CuBi_2O_4$ photocathode through ramping rate control, *Int. J. Hydrogen Energy*, 2020, **45**, 15121–15128.

12 G. Wang, H. Wang, Y. Ling, Y. Tang, X. Yang, R. C. Fitzmorris, C. Wang, J. Z. Zhang and Y. Li, Hydrogen-treated TiO_2 nanowire arrays for photoelectrochemical water splitting, *Nano Lett.*, 2011, **11**, 3026–3033.

13 K. Sivula, F. Le Formal and M. Gratzel, Solar water splitting: progress using hematite (α-Fe_2 O_3) photoelectrodes, *ChemSusChem*, 2011, **4**, 432–449.

14 J. A. Seabold and K.-S. Choi, Effect of a cobalt-based oxygen evolution catalyst on the stability and the selectivity of photo-oxidation reactions of a WO_3 photoanode, *Chem. Mater.*, 2011, **23**, 1105–1112.

15 Y. Park, K. J. McDonald and K. S. Choi, Progress in bismuth vanadate photoanodes for use in solar water oxidation, *Chem. Soc. Rev.*, 2013, **42**, 2321–2337.

16 N. Kornienko, N. A. Gibson, H. Zhang, S. W. Eaton, Y. Yu, S. Aloni, S. R. Leone and P. Yang, Growth and photoelectrochemical energy conversion of wurtzite indium phosphide nanowire arrays, *ACS Nano*, 2016, **10**, 5525–5535.

17 Y. J. Jang, J. W. Jang, S. H. Choi, J. Y. Kim, J. H. Kim, D. H. Youn, W. Y. Kim, S. Han and J.-S. Lee, Tree branch-shaped cupric oxide for highly effective photoelectrochemical water reduction, *Nanoscale*, 2015, **7**, 7624–7631.

18 A. Paracchino, V. Laporte, K. Sivula, M. Gratzel and E. Thimsen, Highly active oxide photocathode for photoelectrochemical water reduction, *Nat. Mater.*, 2011, **10**, 456–461.

19 J. Luo, L. Steier, M. K. Son, M. Schreier, M. T. Mayer and M. Grätzel, Cu_2O nanowire photocathodes for efficient and durable solar water splitting, *Nano Lett.*, 2016, **16**, 1848–1857.

20 H. Lee, W. Yang, J. Tan, Y. Oh, J. Park and J. Moon, Cu-Doped NiO_x as an Effective Hole-Selective Layer for a High-Performance Sb_2Se_3 Photocathode for Photoelectrochemical Water Splitting, *ACS Energy Lett.*, 2019, **4**, 995–1003.

21 L. F. Gao, W. J. Luo, Y. F. Yao and Z. G. Zou, An all-inorganic lead halide perovskite-based photocathode for stable water reduction, *Chem. Commun.*, 2018, **54**, 11459–11462.

22 J.-H. Choi, D. R. Dhakal, Y. K. Kshetri, B. Chaudhary, B. Joshi, S. W. Lee and T.-H. Kim, Role of surfactants on particle deposition, wear, and corrosion behavior of TaC particle incorporated electroless nickel-phosphorus coating, *Prog. Nat. Sci.: Mater. Int.*, 2022, **32**, 655–663.

23 H. Khan, M.-J. Kim, P. Balasubramanian, M.-J. Jung and S.-H. Kwon, Improving the photoelectrochemical stability of a bismuth vanadate photoanode for solar water oxidation, *Cell Rep. Phys. Sci.*, 2023, **4**, 101652.

24 H. Zhang, H. Li, Z. Wang, Z. Zheng, P. Wang, Y. Liu, X. Zhang, X. Qin, Y. Dai and B. Huang, Fabrication of $BiVO_4$ photoanode consisted of mesoporous nanoparticles with improved bulk charge separation efficiency, *Appl. Catal., B*, 2018, **238**, 586–591.

25 T. Carey, C. Jones, F. Le Moal, D. Deganello and F. Torrisi, Spray-coating thin films on three-dimensional surfaces for a semitransparent capacitive-touch device, *ACS Appl. Mater. Interfaces*, 2018, **10**, 19948–19956.

26 C. G. Bruziquesi, M. C. Stolzemburg, R. R. de Souza, M. Rodriguez, M. L. Rocco, P. E. Salomão, A. E. Nogueira, Z. E. López-Cabaña, M. C. Pereira and A. C. Silva, Cobalt as a sacrificial metal to increase the photoelectrochemical stability of $CuBi_2O_4$ films for water splitting, *Int. J. Hydrogen Energy*, 2023, **48**, 3456–3465.

27 S. Bera, S. A. Lee, W.-J. Lee, J.-H. Kim, C. Kim, H. G. Kim, H. Khan, S. Jana, H. W. Jang and S.-H. Kwon, Hierarchical Nanoporous $BiVO_4$ Photoanodes with High Charge Separation and Transport Efficiency for Water Oxidation, *ACS Appl. Mater. Interfaces*, 2021, **13**, 14291–14301.

28 H. Khan, M.-J. Kim, J.-H. Baek, S. Bera, H.-J. Woo, H.-S. Moon and S.-H. Kwon, Sustained water oxidation with surface and interface-engineered $WO_3/BiVO_4$ heterojunction photoanodes, *ACS Appl. Energy Mater.*, 2022, **5**, 15788–15798.

29 H. Khan, A. Razazzadeh, M. Shamekhi, G. Peslherbe, M.-J. Jung, S. Bera and S.-H. Kwon, Tuning Bifunctional Properties of α-Fe_2O_3/Fe_2TiO_5/Pt Heterojunction Photoelectrode for Light-Induced Water Oxidation and Oxygen Reduction Activity, *J. Mater. Chem. A*, 2025, DOI: **10.1039/D5TA01401H**.

30 B. Lei, D. Xu, B. Wei, T. Xie, C. Xiao, W. Jin and L. Xu, In Situ Synthesis of α-Fe_2O_3/Fe_3O_4 Heterojunction Photoanode *via* Fast Flame Annealing for Enhanced Charge Separation and Water Oxidation, *ACS Appl. Mater. Interfaces*, 2021, **13**, 4785–4795.

31 Y. Yang, D. Xu, Q. Wu and P. Diao, Cu_2O/CuO Bilayered Composite as a High-Efficiency Photocathode for Photoelectrochemical Hydrogen Evolution Reaction, *Sci. Rep.*, 2016, **6**, 35158.

